






# High-Q metasurface signal isolator for 1.5T surface coil magnetic resonance imaging on the go

QUN REN,<sup>1,2</sup> YUXIN LANG,<sup>1</sup>  YUQI JIA,<sup>1</sup> XIA XIAO,<sup>3</sup> YU LIU,<sup>3</sup> XIANGZHENG KONG,<sup>3</sup> RUIQI JIN,<sup>1</sup> YUQING HE,<sup>1</sup> JIANAN ZHANG,<sup>2</sup> JIAN WEI YOU,<sup>2</sup>  WEI E. I. SHA,<sup>4</sup>  AND YANWEI PANG<sup>1,\*</sup>

<sup>1</sup>School of Electrical and Information Engineering, Tianjin University, Tianjin 300072, China

<sup>2</sup>State Key Laboratory of Millimeter Waves, School of Information Science and Engineering, Southeast University, Nanjing 210096, China

<sup>3</sup>Tianjin Key Laboratory of Imaging and Sensing Microelectronic Technology, School of Microelectronics, Tianjin University, Tianjin 300072, China

<sup>4</sup>Key Laboratory of Micro-Nano Electronic Devices and Smart Systems of Zhejiang Province, College of Information Science and Electronic Engineering, Zhejiang University, Hangzhou 310027, China

\*pyw@tju.edu.cn

**Abstract:** The combination of surface coils and metamaterials remarkably enhance magnetic resonance imaging (MRI) performance for significant local staging flexibility. However, due to the coupling in between, impeded signal-to-noise ratio (SNR) and low-contrast resolution, further hamper the future growth in clinical MRI. In this paper, we propose a high-Q metasurface decoupling isolator fueled by topological LC loops for 1.5T surface coil MRI system, increasing the magnetic field up to fivefold at 63.8 MHz. We have employed a polarization conversion mechanism to effectively eliminate the coupling between the MRI metamaterial and the radio frequency (RF) surface transmitter-receiver coils. Furthermore, a high-Q metasurface isolator was achieved by taking advantage of bound states in the continuum (BIC) for extremely high-resolution MRI and spectroscopy. An equivalent physical model of the miniaturized metasurface design was put forward through LC circuit analysis. This study opens up a promising route for the easy-to-use and portable surface coil MRI scanners.

© 2024 Optica Publishing Group under the terms of the [Optica Open Access Publishing Agreement](#)

## 1. Introduction

Magnetic resonance imaging (MRI) is widely used in the early diagnosis and screening of systemic tumors and nervous system diseases, due to its noninvasive and high-penetration characteristics [1]. This powerful imaging technology has growing in popularity in clinical devices on the go, becoming an essential tool in early diagnosis and screening of systemic tumors, nervous system, cardiovascular system and other diseases [2,3]. Specifically, signal-to-noise ratio (SNR) is one of the important indexes to evaluate image quality. A higher SNR means higher spatial resolution and faster images, which is the key technology to facilitate future clinical MRI examinations. Therefore, it is of great significance to improve the SNR of MRI, which is possible to be achieved by intelligent magnetic metamaterials with very low cost of upgrading high-end power scanners [4].

The unique properties of metamaterials arise from both the inherent characteristics of their constituent materials and the precise arrangement of their internal structure, offering significant design flexibility, in which MRI is one of the most important application fields [3–5]. One approach to enhance MRI capabilities involves the use of planar metamaterials, including Swiss-roll arrays, split-ring arrays with negative magnetic permeability, and metallic wire arrays [4–6]. Furthermore, advancements have been made in magneto-inductive waveguides and

flexible metamaterial endoscopes for MRI, which have shown the potential to enhance SNR and enable image transmission through curved wire mediums, respectively [7–9]. Nevertheless, it is important to note that while these initial efforts in applying metamaterials to MRI are promising, they currently face challenges in terms of clinical practicality and may not significantly contribute to advancing modern MRI technology. Another type of metamaterial configuration that has been explored is volumetric metamaterials, offering significantly improved magnetic field uniformity compared to planar metamaterials [10,11]. In spite of that, a drawback is their larger size since the length of the wires used in these configurations is typically equal to half the wavelength of the operating frequency. More recently, numerous studies have demonstrated the potential of metamaterials in enhancing the SNR of RF surface coils within MRI systems. Pursuing local surface coil MRI is an appealing alternative to traditional birdcage coil transmission, especially for patients with implants, with substantially enhanced magnetic field, expanded imaging range and greatly improved SNR [12,13].

However, it is inevitable that a certain coupling interaction occurs in between, resulting in reduced signal transmission efficiency, amplified noise and unexpected safety concerns [14,15]. Particularly, an additional magnetic field inhomogeneity might bring about the introduction of artifacts and even image failure [16–18]. Typically, a common method for decoupling to impede mutual interference between signals is through classical shielding [19,20]. However, the combination of surface coils and MRI signal enhancers based on metamaterials is not suitable for this decoupling approach because what we require is achieving simultaneous signal superposition and enhancement between the two while maintaining isolation [21–24]. Indeed, balancing decoupling and MRI signal enhancement has become an important technical challenge. Achieving both objectives simultaneously requires careful consideration and design to optimize the performance of the system [10,25,26].

Here, we report a high-Q metasurface-based decoupling isolator for MRI fueled by surface coils to effectively eliminate this coupling through polarization conversion. While different schemes to manipulate and enhance magnetic fields have been presented, we propose a configuration of a multi-layer decoupling isolator and demonstrate the practicality and efficacy of utilizing it for friendly clinical applications. Moreover, we examine the principles of cross-polarization conversion to clarify the mechanism of the isolator when exposed to incident circular-polarized plane waves. Furthermore, by breaking the symmetry of the metal winding structure, we present the potential to achieve high Q with bound states in the continuum. Lastly, the performance of the decoupling isolator is testified with wrist and leg imaging as examples. As a result, the resonant mode of the metamaterial is excited during the MRI procedure, leading to a marked boost in magnetic field strength.

## 2. Design of decoupling metasurface isolator

The decoupled metasurface isolator excited by circular-polarized signal designed in this paper consists of three cascading layers of unit cell arrays as shown in Fig. 1(a), with the length of 29.48 mm, width of 23.4 mm, and height of 58 mm, respectively. The metal winding ( $w_r = 40.5$  mm,  $g_d = 36$  mm and  $w_d = 3$  mm), was fabricated on both sides of each dielectric substrate, connected with the cuboid metal strips, to realize cross polarization transformation which is essential for decoupling process (the material of the dielectric layer is FR-4, and the dielectric constant is 4.3, the material of the metal winding structure is copper, and the conductivity is  $5.8e^{+7}$  S/m).

In order to explore the decoupling effect and magnetic resonance enhancement of the decoupling isolator, in the following discussion, a topological circuit model of the decoupling process was analyzed via joint simulation of the surface coil and metamaterial. Herein to simplify the process, the surface coil was constructed using a single square metal ring interspersed with capacitors, each featuring 4 evenly spaced notches by  $90^\circ$  intervals. An adjustable capacitor was strategically placed within each gap for tuning frequencies. In the meantime, the metamaterial consisted of

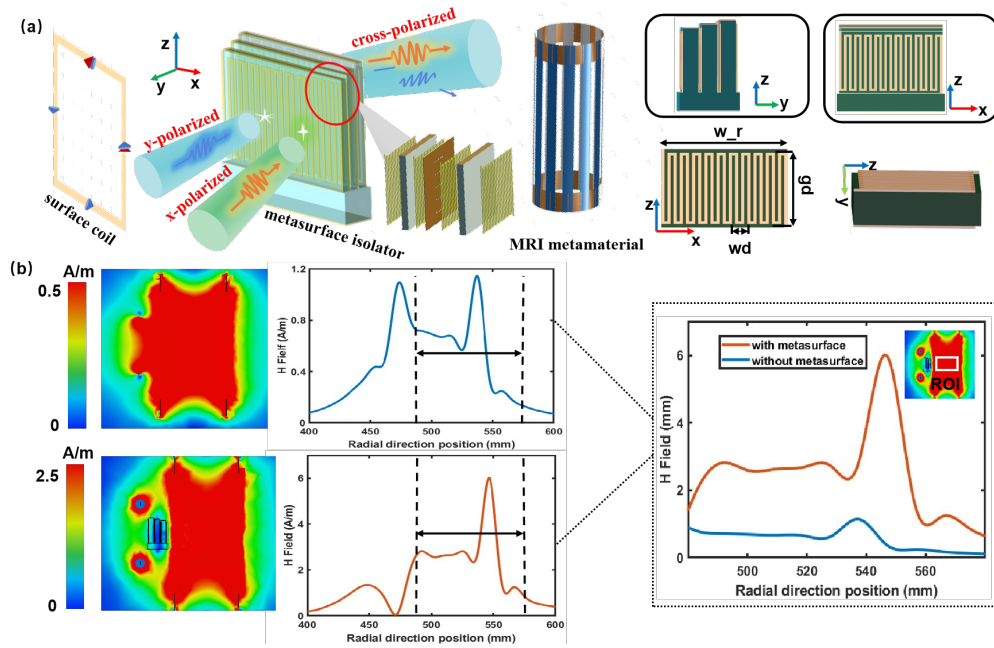


**Fig. 1.** (a) Co-simulation diagram of the MRI enhancement system, with 3-view drawings of decoupling metasurface isolator constructed by topological loops on the right. The metasurface can be divided into three layers, including three dielectric substrates with varying widths (42 mm, 40 mm, 38 mm), along with metal winding wires on both sides of each substrate, placed at a uniform distance of 1.7 mm. (b) Magnetic field enhancement and the radial magnetic field strength distribution spectra with/without the metasurface isolator.

12 strips, each separated by  $30^\circ$  angle. Each strip adopted a three-layer structure, comprising a metal coating at the bottom, a dielectric material in the middle, and metal rings at both ends serving as fixtures and connectors.

Our 1.5T magnetic resonance imaging system was excited by a circular polarized signal, which can be decomposed into two distinct ports with  $90^\circ$  phase difference. A magnetic field probe was placed in the center of the metamaterial at radial coordinate of 530 mm. The magnetic field enhancement and the radial distribution of magnetic field, was presented in Fig. 1(b), within the region of interest (ROI), particularly with radial distribution along Z coordinate (a rectangular region is taken along the middle of the internal radial of the metamaterial to observe the enhanced uniformity of the radial magnetic field). The side view of the magnetic field between the surface coil and metamaterial indicates coupling between these two components, resulting in a reduction of overall magnetic field. Keeping the spacing between the metamaterial and surface coil unchanged, when decoupling metasurface isolator was put in between, the magnetic field enhancement operated at 63.8 MHz can be obviously improved.

It's worth noting that in the absence of decoupling isolator, the magnetic field spectrum exhibits two peaks in the radial direction (as shown in Fig. 1(b) above, at 470mm and 540mm). However, upon introducing the decoupling isolator, the first peak vanishes (as depicted in Fig. 1(b) below), leaving only peak at 540mm. This happens because, in spite of the decoupling isolator there is still some degree of coupling with the metamaterial itself. As a result, there is a reduction in magnetic field strength near the isolator (at 470 mm). Within the inner ROI in Fig. 1(b), as the radial distance increases, both curves consistently demonstrate the same trend, further confirming the decoupling effect achieved by isolator.

The presence of the decoupled metasurface within the metamaterial results in a magnetic field enhancement by 4-6 times, where the most significant enhancement occurs at a radial distance of 550 mm. Consequently, in the joint simulation of all 3 components, the decoupling process between RF coil and MRI metamaterial brings about a collaborative enhancement of the magnetic resonance imaging process.

### 3. Discussion

#### 3.1. Equivalent topological LC circuit of the metasurface isolator

To analyze the electromagnetic behavior of the metal-dielectric hybrid metamaterial, the overall structure can be decomposed into 3 cascaded layers, represented as 'Part1', 'Part2', and 'Part3' in an equivalent circuit, as shown in Fig. 2. An equivalent LC circuit model is established based on the structure of the metasurface isolator. The base layer consists of a bottom metal square patch coupled to a dielectric layer of substrate. This layer not only reflects incident electromagnetic waves but also exhibits bandstop characteristics. On basis of above nature, further winding in the dielectric layer and the adjacent serpentine metal winding structure exhibit bandpass characteristics determined by their slotted design, which can be represented as a parallel combination of inductors and capacitors. The serpentine metal structure sandwiched on both sides can be seen as forming a connected configuration in series. Hereby, for the single-side metal structure, the connection between the two side metal structures is established through upper and lower metal strips to form a series circuit referred to as 'Part1', and so on.

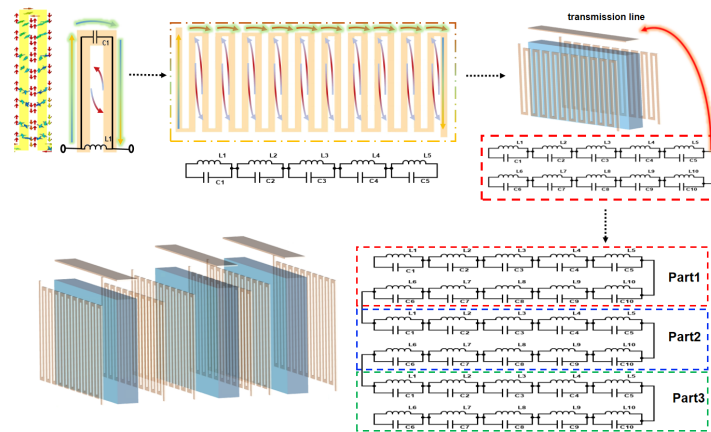


**Fig. 2.** The derivation of an equivalent LC circuit schematic for a three-layer cascaded decoupled metasurface. The current distribution and circuit model of a single-winding structure, a single-layer metal winding structure and double-layer metal winding structure with the addition of the dielectric medium is depicted in the upper left, middle and upper right inset, respectively. Below is the breakdown diagram of the three-level cascaded structure and corresponding circuit model.

The basic principle of the isolator resonance performance is related to the L-C circuit resonance and resonant frequency, and the resonant frequency  $f = \frac{1}{2\pi\sqrt{LC}}$ , where L and C are the equivalent inductance and capacitance, respectively. Inductance L includes the self inductance and mutual inductance of array elements and rings [27]. In the multilayer structure, we analyze each layer of isolator individually to obtain the equivalent circuit of each layer structure and cascade it through the transmission lines [28]. According to the current distribution and electric field distribution of each layer of isolator, an equivalent circuit model of metal-dielectric stacked metamaterials is proposed. Each loop of the dielectric layer and the serpentine metal winding structure on both

sides provides bandpass characteristics due to its slotted structure, so it is modeled by a parallel combination of inductance and capacitance [29]. The serpentine metal structure on each side can be seen as a series form of each loop, so the single-sided metal structure is modeled by series. The metal structure on both sides is connected by the top metal on top and the lower part is connected by metal strips, so it is essentially a series circuit, which is regarded as Part 1. In this way, a total of three layers are cascaded, and the corresponding circuit model is decomposed into series circuits of Part1, Part2, and Part3. In absence of the other metal layers, the square metal patch at the bottom layer consists of metal square patches that reflect incident electromagnetic waves and thus block the electromagnetic wave [30]. Therefore, it is modeled by a series combination of inductors and capacitors to provide band-resistance characteristics. The value of  $C_{bottom}$  for square patches of length  $L$  and metal patches spacing  $h$  is given by [23]:

$$C_{bottom} = \varepsilon_0 \varepsilon_{eff} \frac{2L \log(\operatorname{cosec} \frac{\pi h}{2L})}{\pi}, \quad (1)$$

where  $\varepsilon_0$  is the vacuum permittivity,  $\varepsilon_{eff} = 0.5(1 + \varepsilon_r)$ ,  $\varepsilon_r$  is the permittivity of the dielectric layer,  $L$  is the length of the square patch,  $h$  is the distance from the bottom plate to the dielectric layer. The inductance  $L_{bottom}$  of the square metal patch backed by a single layered dielectric substrate of permittivity  $\varepsilon_r$  is given by:

$$\omega_0 = \frac{1}{2\pi \sqrt{L_{bottom} C_{bottom}}}. \quad (2)$$

For a three-level structure, the capacitance solution formula for each parallel circuit is:

$$C = \frac{\varepsilon_{eff}(N-1)D}{18\pi} \frac{K(k)}{K'(k)}, \quad (3)$$

where  $K(k)$  is the complete elliptic integral of the first kind and its complement is  $K'(k)$ ,  $D$  is the length of the metal bar of the serpentine metal structure,  $N$  is the number of metal bars.

Herein,

$$\frac{K(k)}{K'(k)} = \begin{cases} \frac{1}{\pi} \ln \left[ \frac{2(1+\sqrt{k})}{1-\sqrt{k}} \right] & \text{for } 0.707 \leq k \leq 1 \\ \frac{\pi}{\ln[2(1+\sqrt{k'})(1-\sqrt{k'})]} & \text{for } 0 \leq k \leq 0.707 \end{cases} \quad (4)$$

and

$$k = \tan^2\left(\frac{a\pi}{4b}\right), a = \frac{w_d}{2}, b = \frac{w_d + g_d}{2}, k' = \sqrt{1 - k^2} \quad (5)$$

where  $w_d$  is the width of each metal winding and  $g_d$  is the length of the metal-winding wire.

The inductance continues to be solved using Eq. (2). Finally, the equivalent capacitance of the entire circuit model is 89 pF and the equivalent inductance is 70 nH, which meets the requirement of 63.8 MHz resonance frequency in 1.5 T magnetic resonance system.

### 3.2. Underlying physics of decoupling process

After the incident x-polarized and y-polarized waves pass through the decoupling isolator, the transmitted waves become orthogonal waves (y-polarized and x-polarized waves, respectively), so as to reduce the coupling between surface coil and MRI metamaterial and superimpose the mode vectors of both. According to the polarization conversion principle of metasurface isolator, the electric field distribution of the metal winding structure during the conversion of x-polarized wave and y-polarized wave is further analyzed [31]. The principle analysis is shown in Fig. 3(a). The uv coordinate system is the relative coordinate system obtained through rotating the xy coordinate system by 45 degree counterclockwise to resolve the incident electromagnetic wave into the uv direction [32]. The polarization rotation of transmitted electromagnetic wave is easy



to observe then in this way. Specifically, the incident electromagnetic wave can be expressed by the following formula [33]:

$$\mathbf{E}_i = v\mathbf{E}_{iv}e^{j\varphi_{iv}} + u\mathbf{E}_{iu}e^{j\varphi_{iu}} \quad (6)$$

where  $\mathbf{E}_i$  represents the incident linear polarized wave,  $\mathbf{E}_{iv}$  and  $\mathbf{E}_{iu}$  indicate the incident wave amplitude in the  $v$  and  $u$  direction, and  $v, u$  indicate the unit vector in the  $v$  and  $u$  directions, respectively.  $e^{j\varphi_{iu}}$  and  $e^{j\varphi_{iv}}$  are the phase of the two incident wave components, respectively.

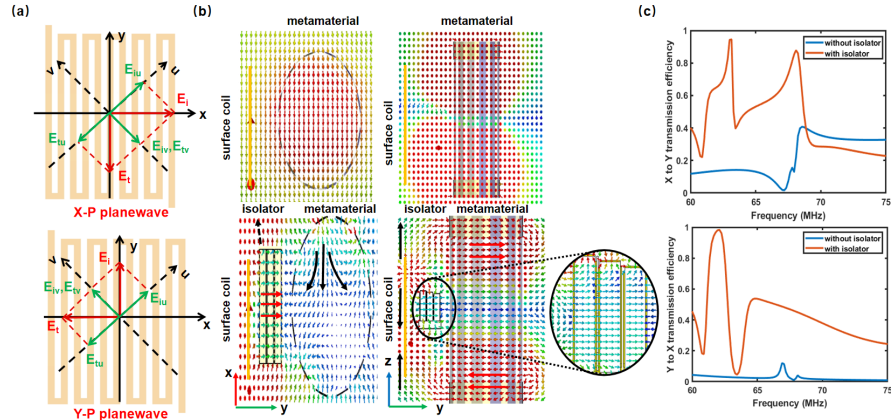


**Fig. 3.** (a) Decomposition of electromagnetic waves on a single layer serpentine metal structure in the  $uv$  coordinate system, where the left incident wave is x-polarized and the right one is y-polarized. (b) Schematic diagram of the current direction. The top is the result when no isolator is added. It can be seen that the current direction on the surface coil and MRI metamaterial is the same in the  $x$  direction. Below is the result of adding the isolator. The current on the surface coil is in the  $z$  direction, while the current on the metamaterial is in the  $y$  direction, so that the electric field becomes orthogonal by passing the isolator. This proves the orthogonal polarization conversion process of the isolator. (c) Polarization conversion ratio (PCR) result in the MRI operating band. Above is the conversion efficiency of x-polarized wave to y-polarized wave, whereas below is the conversion efficiency of y-polarized wave to x-polarized wave.

The transmitted wave can be expressed as follows:

$$\mathbf{E}_t = t_v\mathbf{E}_{tv}e^{j\varphi_{tv}} + t_u\mathbf{E}_{tu}e^{j\varphi_{tu}} \quad (7)$$

In Eq. (7),  $\mathbf{E}_t$  is the transmitted wave,  $t_v$  and  $t_u$  represents the transmission efficiency of the electric field components in both directions,  $e^{j\varphi_{tv}}$  and  $e^{j\varphi_{tu}}$  are the phases of these two transmitted wave components, respectively.

As shown in Fig. 3(b), the decomposition of the electric field, when the incident wave incident along the  $x$ -axis direction, because of the presence of the serpentine metal winding vertical bars on the left and right sides, the electric field component in the  $u$  direction changes in direction  $180^\circ$ , if  $t_u \approx t_v$  at this time, the direction of the resultant transmission wave direction is the  $y$ -axis direction, which makes the  $\mathbf{E}_t$  linear polarization wave conversion to design cross polarization [34]. When the incident wave is y-polarized wave, can be found that the unit structure along the  $y$  axis is positive direction and negative direction are two metal structure, so the electromagnetic wave and metal structure coupling, decomposition of the component on the  $uv$  direction,  $u$  direction of the electric field also of  $180^\circ$  direction change, combined behind the analysis, can find y-polarized wave incident, electromagnetic wave basically all the cross transmission transition [35,36]. The case shown in Fig. 3(c) is the simulation result obtained from the negative direction of the incident wave, that is, the vertical incident from the front of the metasurface, which is

divided into two cases: the incident wave is x-polarized (PCR1) and y-polarized (PCR2). The PCR in Fig. 3 can be defined as [37]:

$$PCR = |T_{xy}|^2 / (|T_{xy}|^2 + |T_{yy}|^2) \quad (8)$$

$T_{xx}$  and  $T_{yy}$  are transmission coefficients of isopolarization under the front or reverse incident, respectively,  $T_{xy}$  and  $T_{yx}$  are transmission coefficients of cross polarization under the front or reverse incident, respectively. To further understand the conversion physics of this multilayer structure, which means a  $90^\circ$  change will be achieved when the polarization direction of the incident EM wave is along the y-axis(or x-axis), we first define the polarization direction is along y-axis for instance, then the cross- and co-polarization can be depressed as  $T_{xy} = |E_{xt}/E_{yt}|$  and  $T_{yy} = |E_{yt}/E_{yt}|$  respectively, where E indicates the electric field; the subscript i and r defines the incidence and transmission of EM waves, respectively; and the subscripts x and y denote the polarization directions of EM waves, respectively [14,15].

To assess the polarization transformation effect of the proposed isolator, we conducted a comprehensive analysis through both electric field characterization and the calculation of the PCR. In Fig. 3(b), we present the electric field distribution map, providing top and side views. In the top view, shown on the left, we present the results without incorporating the isolator, demonstrating that the electric field consistently aligns with the x-axis. This consistency holds true on both the surface coil side and within the metamaterials region. Conversely, in the bottom view, after introducing the isolator, a conspicuous orthogonal polarization conversion effect becomes evident. The electric field on the surface coil shifts towards the z-axis, while significant orthogonal changes occur post-isolator integration, resulting in a shift towards the y-axis. Additionally, the electric field within the metamaterial now aligns with the isolator direction, extending along the y-axis. This observation leads us to conclude that the isolator effectively decouples the system by orthogonal electric field direction conversion. This conversion establishes orthogonality between the electric field orientations on the surface coil side and the metamaterial side, resulting in a substantial reduction in coupling losses and a notable enhancement in polarization conversion efficiency.

Figure 3(c) illustrates the PCR as a function of frequency. The upper section represents the conversion efficiency of x-polarized waves to y-polarized waves, while the lower section illustrates the conversion efficiency of y-polarized waves to x-polarized waves. Remarkably, at a frequency of 63.8 MHz, the PCR calculated after incorporating the isolator consistently exceeds 80%, in stark contrast to the PCR observed without the isolator, which remains low, typically below 20%, which underscores the remarkable performance enhancement achieved with the isolator integration. In essence, this indicates that over the extensive frequency range, both x-polarized and y-polarized incident electromagnetic waves consistently exhibit an approximate 90-degree phase shift, affirming the isolator effectiveness in achieving polarization orthogonality.

### 3.3. Realization of ultra high Q factors

In this section, symmetry-protected BIC is formed by breaking the structural symmetry within the system to achieve high Q factor. When a state exhibits different symmetry characteristics compared to its surroundings, it is decoupled from radiation and behaves as BIC. This unique state, known as a symmetry-protected BIC, maintains its localization as long as the system symmetry remains unchanged [38,39]. The distinguishing feature of symmetry-protected BICs is their predictability, which avoids fine-tuning structural parameters in wave vector space to locate them, which have been extensively studied across various systems, including metasurfaces, sub-wavelength structures, classical gratings, and photonic crystals [40,41].

Since BICs represent discrete modes effectively decoupled from the radiation continuum of different symmetric classes, when these discrete modes are excited in an asymmetric manner, their electromagnetic field distributions deviate from the symmetry mode, leading to the emergence

of ultra-high Q resonances [41–43]. The extent of leakage resonance depends on the degree of structural asymmetry [44–47]. By introducing periodic perturbations in the direction or position of adjacent elements, in-plane symmetry can be broken, even at oblique or positive incidence angles, allowing these modes to leak into free space [48–50].

Hereby, we introduce a metasurface achieving a high Q-factor BIC in the cross-polarization configuration. Initially, in the case of symmetry on the left and right sides of the metal winding structure, there is no resonant peak in the spectral response. Then, we break the symmetry of the structure and reduce the length of the leftmost metal strip, and the amplitude of the reduction, that is, the length difference between the left and right metal bars, is expressed by  $\Delta L$ . When the length of the right metal strip is reduced to 1 mm, the transmittance decreases significantly at 140 MHz and an unexpected quasi-BIC is excited, regarded as BIC1. However, the BIC1 frequency does not meet the frequency band requirement of 1.5 T magnetic resonance system. Continue to reduce the length of the right metal bar, and when the gap increases to 8 mm, a clear transmission valley can be observed on the transmission spectrum of 63.8 MHz, i.e., BIC2. In this case, BIC1 moves to lower frequency. Symmetry-protected BIC can be verified by breaking the structural symmetry of the device. We demonstrate the quasi-BIC phenomenon caused by symmetry fracture of metal winding structure, which has 6 different degrees of fracture, and the asymmetric transition from symmetry-protected BIC to quasi-BIC can be observed from the simulated transmission spectrum in the Fig. 4(a). The spectral properties of quasi-BICs also depend on the size of the symmetry break  $\Delta L$ .

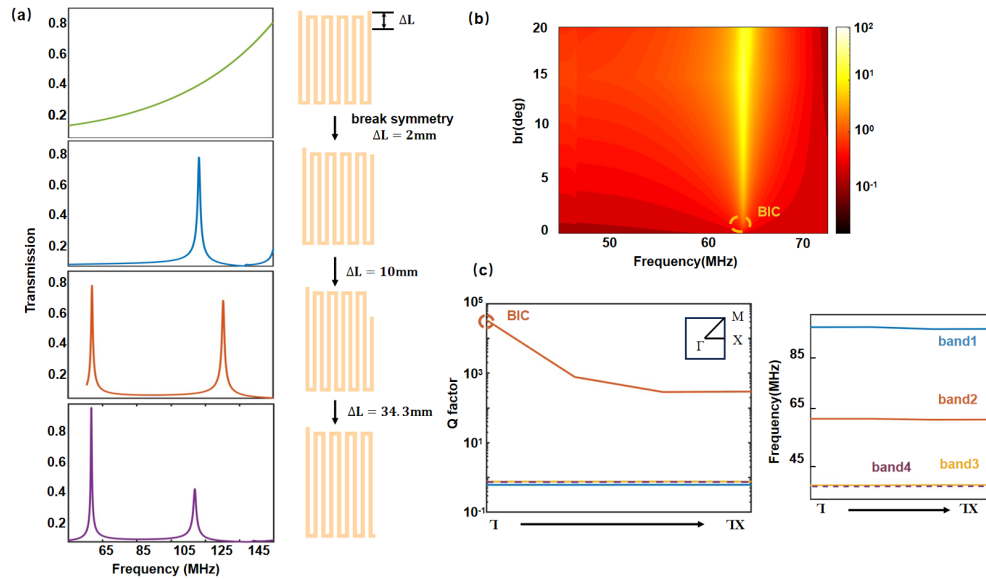


**Fig. 4.** (a) Transmission spectra for  $\Delta L = 0$  mm, 2 mm and 10 mm. (b) Discrete spectra and color plot of simulated transmission spectra with different  $\Delta L$ , changing  $\Delta L$  from 0 mm to 20 mm. (c) Corresponding Q factor and band structure for the BIC.

The disappearance of the resonance of the symmetric recovery region proves symmetry-protected BIC, where the Fig. 4(b) of merit tends to infinity as the symmetrical gap of the broken symmetry becomes zero. The transmission response of metal wound structures with different clearances ( $\Delta L$ ) was scanned. When the symmetry is broken, a clear quasi-BIC phenomenon can be seen at  $\Delta L = 8$  mm. For an ideal BIC, the theoretical merit factor should be close to infinity when the imaginary part of the permittivity is zero. However, the inherent losses in metal lead to limited quality factors in depleted BICs. The left of Fig. 4(c) shows the Q factor calculated by this



method to break the symmetry and symmetric structure at about 63.8 MHz, and shows that the Q factor of the quasi-BIC calculated at the symmetry point rises rapidly, indicating that the point is aligned with the protection of the BIC. The right of Fig. 4(c) shows a possible characteristic pattern at 63.8MHz in the  $\Gamma - \Gamma X$  direction.

#### 4. MRI at 1.5T for a set of body phantoms

A set of body phantoms of different genders and ages representing various human tissue properties are simulated at 1.5T MRI condition. The dimensions of the phantom are available to the co-simulation system. An RF surface coil is employed to generate a circularly polarized magnetic field (B1). Two excitation sources with a 90° phase difference are placed at positions differing by 90°, applying their excitation at the Larmor frequency in a counter-parallel and perpendicular manner to the static magnetic field [51].

The primary function of the surface coil in the MRI system is to excite unpaired proton spins of hydrogen atoms at the Larmor frequency during the transmit mode and to receive signals emitted by these protons at the same Larmor frequency during the receive mode [51]. Following the reciprocity principle, a simplified square-shaped surface coil is designed to operate exclusively in the receive mode, as shown in Fig. 1(a). The coil consists of a square metal loop with 4 equally spaced 90° wide gaps, each housing a tunable capacitor of 24 pF to tune the surface coil for matching the spin's Larmor frequency. Copper traces with a width of 0.5 mm are used to excite the phantom at 63.8 MHz. The coil is placed at a distance of 50 mm from the metamaterial. Due to resonance scattering of the RF field and spatial redistribution of the electromagnetic field near the metamaterial at its resonance frequency, magnetic field enhancement occurs. This resonance frequency matches the Larmor frequency of 1.5T MRI. The incident electromagnetic field experiences macroscopic effects due to the interaction between the surface coil and the metamaterial. When the RF wave impinges on the metamaterial, induced currents in the metal patches of each unit cell are observed. At resonance, the decoupling metamaterial produces enhanced magnetic flux density in the region of interest within the metamaterial.

Due to the slight resonance frequency shift observed after introducing the phantom in joint simulations, we add a monitor at the Larmor frequency after including the phantom, used to observe the magnetic field distribution curves and magnetic field enhancement effects at the resonance frequency. Figure 5(a) depicts the frequency-dependent magnetic field enhancement curves before and after the inclusion of the phantom. It is evident that prior to adding the phantom, the field strength at the resonance frequency of 63.8 MHz is 10 A/m. However, after introducing the phantom, the resonance frequency shifts to 64.8 MHz, with a field strength of 8 A/m. In Fig. 5(b), precisely at 63.8 MHz, the magnetic field enhancement, occurring during the receive phase after adding the phantom, are illustrated. The standard magnetic field value within the phantom with the isolator remains 2.5 A/m, matching the scenario without the phantom as shown in Fig. 1(b). It can be seen from the distribution diagram of each radial magnetic field curve in Fig. 5(b), the decoupling metamaterial enhances the magnetic field during the receive phase, mitigating field inhomogeneity.

In Fig. 5(b), the distribution results of magnetic field curves along the Z axis are derived. The top image displays the magnetic field strength distribution for the lady's arm during transmission, where the body phantom part shows an obvious magnetic field strength of approximately 3 A/m. In the imaging map of the men's arm, the magnetic field strength for the arm part is around 4 A/m. The leg imaging is less effective compared to the arm imaging due to the limitations of the metamaterial structure used, which has a restricted internal diameter and is more suitable for medical imaging of organs with smaller diameters. As can be seen, the imaging result of women's leg shows that the magnetic field strength at the phantom is about 1.3 A/m, while that of men's leg is about 1.2 A/m. These results demonstrate that the addition of the decoupling isolator significantly improves the enhancement effect of the metamaterial compared to using

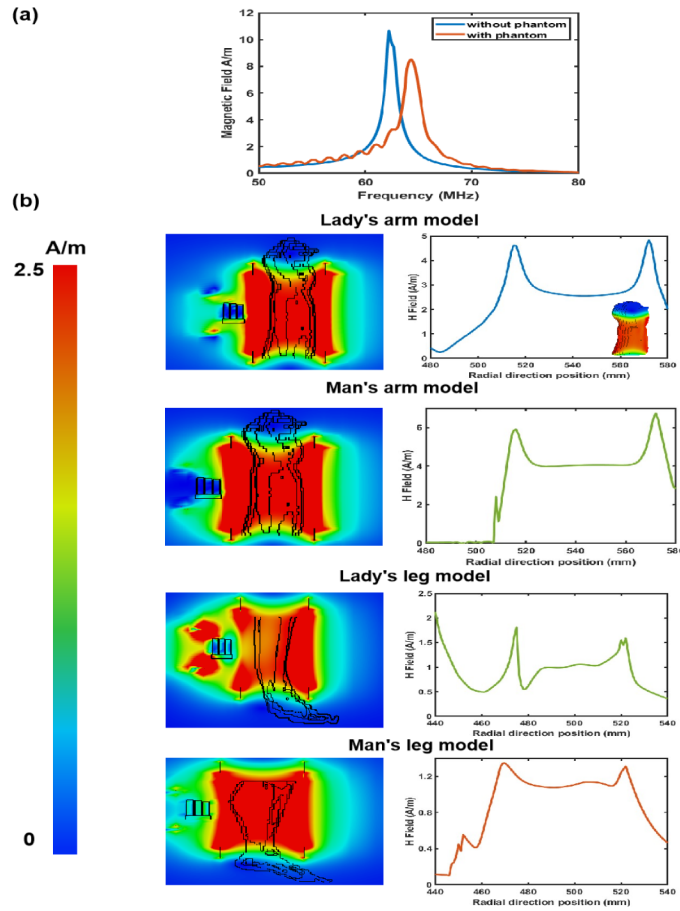


**Fig. 5.** (a) The magnetic field intensity curves before adding the isolator (blue curve) and after adding the isolator (red curve). (b) Magnetic field enhancement diagram and the magnetic field distribution with radial distance after adding the mannequin (arm). The baseline of the 2D magnetic field enhancement rendering on the left is set at 2.5 A/m.

only a surface coil and the metamaterial. Additionally, the coupling between the two is greatly reduced, leading to improved performance.

## 5. Conclusion

This work provides an efficient approach to design a high-Q metasurface decoupling isolator for 1.5T surface coil magnetic resonance imaging. With the multilayer construction, it is possible to ensure a homogeneous field distribution and circular polarization conversion, not only eliminating the coupling between surface coil and metamaterial, but also achieving high-Q value by taking advantage of BIC for extremely high field MRI. The promising results from the study of the decoupling isolator indicate the possibility of applications to all clinical sequences and much higher SNR enhancement and resolution. The frequency shift problem in MRI imaging at 1.5T is expected to be automatically tuned by artificial intelligence in the future, which provides a new direction for the research of MRI in the field of artificial intelligence [52,53].

**Funding.** Open Fund of State Key Laboratory of Millimeter Waves, Southeast University (K202216); National Natural Science Foundation of China (12104339, 52227814); National Key Research and Development Program of China (2023YFC2411100).

**Disclosures.** The authors declare no conflicts of interest.

**Data availability.** No data were generated or analyzed in the presented research.

## References

1. A. Cho, "MRI for all," *Science* **379**(6634), 748–751 (2023).
2. A. Webb and J. Obungoloch, "Five steps to make MRI scanners more affordable to the world," *Nature* **615**(7952), 391–393 (2023).
3. Z. Chi, Y. Yi, Y. Wang, *et al.*, "Adaptive cylindrical wireless metasurfaces in clinical magnetic resonance imaging," *Adv. Mater.* **33**(40), 2102469 (2021).
4. K. Wu, X. Zhao, T. G. Bifano, *et al.*, "Auxetics-inspired tunable metamaterials for magnetic resonance imaging," *Adv. Mater.* **34**(6), 2109032 (2022).
5. N. Wu, Y. Zhang, H. Ma, *et al.*, "Tunable high-q plasmonic metasurface with multiple surface lattice resonances," *Prog. Electromagn. Res.* **172**, 23–32 (2021).
6. G. Duan, X. Zhao, S. W. Anderson, *et al.*, "Boosting magnetic resonance imaging signal-to-noise ratio using magnetic metamaterials," *Commun. Phys.* **2**(1), 35 (2019).
7. M. Koutsoupidou, S. C. Saha, and R. L. Pricci, "Metasurface Resonator for 1.5 T MRI Based on BaTiO<sub>3</sub> Host Material," *2019 41st Annual International Conference of the IEEE Engineering in Medicine and Biology Society (EMBC)*, 6810–6813 (2019).
8. T. Han, K. Wen, Z. Xie, *et al.*, "An ultra-thin wideband reflection reduction metasurface based on polarization conversion," *Prog. Electromagn. Res.* **173**, 1–8 (2022).
9. Q. Ren, J. W. You, and N. C. Panoiu, "Large enhancement of the effective second-order nonlinearity in graphene metasurfaces," *Phys. Rev. B* **99**(20), 205404 (2019).
10. H. Chen, L. Guo, M. Li, *et al.*, "Metamaterial-inspired radiofrequency (RF) shield with reduced specific absorption rate (SAR) and improved transmit efficiency for UHF MRI," *IEEE Trans. Biomed. Eng.* **68**(4), 1178–1189 (2020).
11. A. P. Slobozhanyuk, A. N. Poddubny, A. J. E. Raaijmakers, *et al.*, "Enhancement of magnetic resonance imaging with metasurfaces," *Adv. Mater.* **28**(9), 1832–1838 (2016).
12. J. M. Algarin, M. A. Lopez, M. J. Freire, *et al.*, "Signal-to-noise ratio evaluation in resonant ring metamaterial lenses for MRI applications," *New J. Phys.* **13**(11), 115006 (2011).
13. Q. Ren, F. Feng, X. Yao, *et al.*, "Multiplexing-oriented plasmon-MoS<sub>2</sub> hybrid metasurfaces driven by nonlinear quasi bound states in the continuum," *Opt. Express* **29**(4), 5384–5396 (2021).
14. Q. Ren, J. You, and N. C. Panoiu, "Giant enhancement of the effective raman susceptibility in metasurfaces made of silicon photonic crystal nanocavities," *Opt. Express* **26**(23), 30383 (2018).
15. I. Issa, K. L. Ford, M. Rao, *et al.*, "A magnetic resonance imaging surface coil transceiver employing a metasurface for 1.5 T applications," *IEEE Trans. Med. Imaging* **39**(4), 1085–1093 (2019).
16. H. Chen, J. Wang, H. Ma, *et al.*, "Broadband perfect polarization conversion metasurfaces," *Chin. Phys. B* **24**(1), 014201 (2015).
17. P. Naseri, S. A. Matos, J. R. Costa, *et al.*, "Dual-band dual-linear-to-circular polarization converter in transmission mode application to K/Ka-band satellite communications," *IEEE Trans. Antennas Propag.* **66**(12), 7128–7137 (2018).
18. X. Lai, Q. Ren, F. Vogelbacher, *et al.*, "Bioinspired quasi-3d multiplexed anti-counterfeit imaging via self-assembled and nanoimprinted photonic architectures," *Adv. Mater.* **34**(3), 2107243 (2022).
19. D. Brizi and A. Monorchio, "An analytical approach for the arbitrary control of magnetic metasurfaces frequency response," *Antennas Wirel. Propag. Lett.* **20**(6), 1003–1007 (2021).
20. S. Chen, Q. Ren, K. Zhang, *et al.*, "A highly sensitive and flexible photonic crystal oxygen sensor," *Sens. Actuators, B* **355**, 131326 (2022).
21. A. A. Hurshkainen, T. A. Derzhavskaya, S. B. Glybovski, *et al.*, "Element decoupling of 7 T dipole body arrays by EBG metasurface structures: Experimental verification," *J. Magn. Reson.* **269**, 87–96 (2016).
22. I. Issa, K. L. Ford, M. Rao, *et al.*, "Enhancement of radio frequency magnetic field for a 1.5 T magnetic resonance system using a high impedance surface," *IET Microwaves* **10**(13), 1378–1383 (2016).
23. Q. Cheng, W. Jiang, and T. Cui, "Radiation of planar electromagnetic waves by a line source in anisotropic metamaterials," *J. Phys. D: Appl. Phys.* **43**(33), 335406 (2010).
24. R. Schmidt and A. Webb, "Metamaterial combining electric-and magnetic-dipole-based configurations for unique dual-band signal enhancement in ultrahigh-field magnetic resonance imaging," *ACS Appl. Mater. Interfaces* **9**(40), 34618–34624 (2017).
25. E. Razzicchia, P. Lu, W. Guo, *et al.*, "Metasurface-enhanced antennas for microwave brain imaging," *Diagnostics* **11**(3), 424 (2021).
26. Z. Lin, L. Huang, Z. Xu, *et al.*, "Fourwave mixing holographic multiplexing based on nonlinear metasurfaces," *Adv. Opt. Mater.* **7**(21), 1900782 (2019).
27. Z. Zhang, S. Liang, F. Li, *et al.*, "Spin-orbit coupling in photonic graphene," *Optica* **7**(5), 455 (2020).

28. S. K. Joshi, D. Aktas, S. Wengerowsky, *et al.*, "A trusted node-free eight-user metropolitan quantum communication network," *Sci. Adv.* **6**(36), eaba0959 (2020).
29. K. Wei and A. S. Daryoush, "Hybrid modeling and design optimization of chip level of  $\mu$ s long optical delays for realization of integrated optoelectronic circuits," *Prog. Electromagn. Res.* **172**, 1–12 (2021).
30. Y. Zhang, Y. Guo, X. Kong, *et al.*, "Improving local SNR of a single-channel 54.6mT MRI system using additional LC-resonator," *J. Magn. Reson.* **339**, 107215 (2022).
31. F. Ding, "A Review of Multifunctional Optical Gap-Surface Plasmon Metasurfaces," *Prog. Electromagn. Res.* **174**, 55–73 (2022).
32. H. Fujita, T. Zheng, X. Yang, *et al.*, "RF surface receive array coils: the art of an LC circuit," *J. Magn. Reson. Imaging* **38**(1), 12–25 (2013).
33. W. Peake, "Interaction of electromagnetic waves with some natural surfaces," *IRE Trans. Antennas Propag.* **7**(5), 324–329 (1959).
34. B. J. Paul and S. Mridula, "Ultra-compact band-pass filter at low frequency of operation," *Prog. Electromagn. Res. Lett.* **111**, 17–25 (2023).
35. A. H. Dorrah, N. A. Rubin, A. Zaidi, *et al.*, "Metasurface optics for on-demand polarization transformations along the optical path," *Nat. Photonics* **15**(4), 287–296 (2021).
36. C. Huang, C. Zhang, J. Yang, *et al.*, "Reconfigurable metasurface for multifunctional control of electromagnetic waves," *Adv. Opt. Mater.* **5**(22), 1700485 (2017).
37. P. Das, J. Gupta, D. Sikdar, *et al.*, "A thin metallo-dielectric stacked metamaterial as "add-on" for magnetic field enhancement in clinical MRI," *J. Appl. Phys.* **132**(11), 114901 (2022).
38. N. Wang and S. He, "A simple graphic method for analyzing the polarization state of an optical system with a fixed polarizer and a rotating elliptical retarder," *Prog. Electromagn. Res.* **174**, 107–114 (2022).
39. W. E. I. Sha, W. C. H. Choy, and W. C. Chew, "Theoretical studies of plasmonic effects in organic solar cells," *Organic Solar Cells, Materials and Device Physics* 177–210 (2013).
40. Y. Fan, F. Zhang, N. H. Shen, *et al.*, "Achieving a high-Q response in metamaterials by manipulating the toroidal excitations," *Phys. Rev. A* **97**(3), 033816 (2018).
41. C. W. Hsu, B. Zhen, A. D. Stone, *et al.*, "Bound states in the continuum," *Nat. Rev. Mater.* **1**(9), 16048 (2016).
42. K. Koshelev, A. Bogdanov, and Y. Kivshar, "Meta-optics and bound states in the continuum," *Sci. Bull.* **64**(12), 836–842 (2019).
43. S. I. Azzam and A. V. Kildishev, "Photonic bound states in the continuum: from basics to applications," *Adv. Opt. Mater.* **9**(1), 2001469 (2021).
44. X. Yonghui, Z. Zhenyu, L. Peiliang, *et al.*, "The impact of contact and contactless interaction between the meta-atoms on terahertz bound state in the continuum," *J. Phys. D: Appl. Phys.* **57**(5), 055103 (2023).
45. Z. Zhenyu, D. Mingjie, J. Chunping, *et al.*, "Terahertz inner and outer edge modes in a tetramer of strongly coupled spoof localized surface plasmons," *Opt. Lett.* **48**(6), 1343–1346 (2023).
46. D. Mingjie, Z. Zhenyu, Q. Hua, *et al.*, "Dual band symmetry-protected terahertz bound states in the continuum inside the spoof localized surface plasmon induced-transparency windows," *J. Phys. D: Appl. Phys.* **56**, 045104 (2022).
47. W. Lei, Z. Zhenyu, D. Mingjie, *et al.*, "Tuning symmetry-protected quasi bound state in the continuum using terahertz meta-atoms of rotational and reflectional symmetry," *Opt. Express* **30**(13), 23631–23639 (2022).
48. W. Lei, Z. Zhenyu, D. Mingjie, *et al.*, "Polarization insensitive symmetry protected quasi-bound states in the continuum at terahertz band," *J. Appl. Phys.* **130**(23), 233102 (2021).
49. A. Cerjan, C. Jörg, S. Vaidya, *et al.*, "Observation of bound states in the continuum embedded in symmetry bandgaps," *Sci. Adv.* **7**(52), eabk1117 (2021).
50. P. Das, J. Gupta, D. Sikdar, *et al.*, "Aperture-patch sandwich metasurface for magnetic field enhancement in 1.5 T MRI," *Magn. Reson. Imaging* **100**, 1–9 (2023).
51. A. V. Shchelokova, A. P. Slobozhanyuk, P. de Bruin, *et al.*, "Experimental investigation of a metasurface resonator for in vivo imaging at 1.5T," *J. Magn. Reson.* **286**, 78–81 (2018).
52. Y. Wang, Y. Pang, and C. Tong, "Dsnet: Detail and structure mutually enhancing network for under-sampled MRI reconstruction," *Comput. Biol. Med.* **154**, 106204 (2023).
53. Y. Liu, Y. Pang, X. Liu, *et al.*, "Diik-net. A full-resolution crossdomain deep interaction convolutional neural network for MR image reconstruction," *Neurocomputing* **517**, 213–222 (2023).